Band Edge Energetics of Heterostructured Nanorods: Photoemission Spectroscopy and Waveguide Spectroelectrochemistry of Au-Tipped CdSe Nanorod Monolayers

Ramanan Ehamparam,[†] Nicholas G. Pavlopoulos,[†] Michael W. Liao,[†] Lawrence J. Hill,[†] Neal R. Armstrong,[*,†] Jeffrey Pyun,[*,†,‡] and S. Scott Saavedra[*,†]

[†]Department of Chemistry and Biochemistry, University of Arizona, Tucson, Arizona 85721, United States and [‡]World Class University Program for Chemical Convergence for Energy and Environment, School of Chemical and Biological Engineering, Seoul National University, Seoul 151-744, Korea

ABSTRACT Conduction and valence band energies (E_{CB}, E_{VB}) for CdSe nanorods (NRs) functionalized with Au nanoparticle (NP) tips are reported here, referenced to the vacuum scale. We use (a) UV photoemission spectroscopy (UPS) to measure E_{VB} for NR films, utilizing advanced approaches to secondary electron background correction, satellite removal to enhance spectral contrast, and correction for shifts in local vacuum levels; and (b) waveguide-based spectroelectrochemistry to measure E_{CB} from onset potentials for electron injection into NR films tethered to ITO. For untipped CdSe NRs, both approaches show $E_{VB} = 5.9-6.1$ eV and $E_{CB} = 4.1-4.3$ eV. Addition of Au tips alters the NR band edge energies and introduces midgap states, in ways that are predicted to influence the efficiency of these nanomaterials as photoelectrocatalysts. UPS results show that Au tipping shifts E_{VB} closer to vacuum by up to 0.4 eV, shifts the apparent Fermi energy toward the middle of the band gap, and introduces additional states above E_{VB}. Spectroelectrochemical results confirm these trends: Au tipping shifts E_{CB} closer to vacuum, by 0.4—0.6 eV, and introduces midgap states below E_{CB}, which are assigned as metal—semiconductor interface (MSI) states. Characterization of these band edge energies and understanding the origins of MSI states is needed to design energy conversion systems with proper band alignment between the light absorbing NR, the NP catalyst, and solution electron donors and acceptors. The complementary characterization protocols presented here should be applicable to a wide variety of thin films of heterogeneous photoactive nanomaterials, aiding in the identification of the most promising material combinations for photoelectrochemical energy conversion.

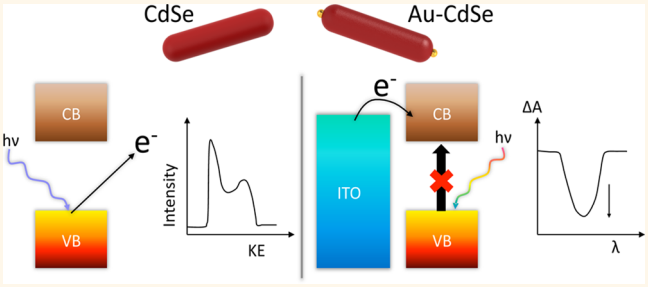

KEYWORDS: semiconductor nanorods · metal nanoparticle · UV photoemission · spectroelectrochemistry · electron transfer · band edge energies

Multicomponent inorganic nanocomposite materials have generated considerable recent interest since the combination of different materials (*e.g.*, metals and II—VI semiconductors) at the nanoscale creates heterojunctions with energetic offsets that enhance their optical, electronic, magnetic and/or photocatalytic properties.[1−8] These enhancements most often occur in lower symmetry constructs, *e.g.*, nanorods (NRs) *vs* nanoparticles (NPs) or quantum dots, since internal potential energy gradients can be developed that, for example, enhance efficiency of charge separation and charge transport *vs* recombination.[1,2,6,9−21] Understanding the energetic impact of heterojunction formation in NR materials (*e.g.*, shifts in valence band (E_{VB}) and conduction band (E_{CB}) energies upon addition of metal or metal oxide tips) is a complex endeavor, preferably addressed using two or more complementary measurement approaches.

Banin and co-workers demonstrated the first synthesis of heterostructured metal—semiconductor NRs by depositing metallic Au NPs onto the termini of cadmium selenide (CdSe) NRs.[5,22] Au NPs selectively

* Address correspondence to saavedra@email.arizona.edu, jpyun@email.arizona.edu, nra@email.arizona.edu.

Received for review March 20, 2015 and accepted August 20, 2015.

Published online August 20, 2015
10.1021/acsnano.5b01720

deposit at the NR termini due to their high surface free energy and lower coverage of passivating ligands, but it is clear that this is also critically dependent upon temperature, metal precursor concentration, NR concentration, and passivating ligand type and coverage.[22] The electronic coupling between these "Au tips" and CdSe NRs was subsequently confirmed using conductive tip atomic force microscopy (CAFM), scanning tunneling spectroscopy (STS) and electrostatic force microscopy (EFM), comparing the bare NRs[23] with the Au-tipped NRs.[1,6] STS of the bare NRs on highly ordered pyrolytic graphite substrates (HOPG) showed clean energy gap regions, with band gap energies that were dependent upon NR diameter (up to *ca*. 3−4 nm) and independent of rod length.[23] Addition of a Au tip at both ends of CdSe NRs produced "metal−semiconductor interface" (MSI) states within the band gap that could be detected within 1−2 nm of the Au tip (on a NR with a length of *ca*. 15−40 nm), suggesting an "interphase" region at the CdSe/Au heterojunction with unique electronic properties.[6] At the center of the NR, however, the band gap and the relative valence band and conduction band energies appeared to be largely unchanged from those of the bare NR. Estimates of E_{VB} and E_{CB} referenced to the vacuum scale were not obtainable. Manna and co-workers subsequently used transmission electron microscopy (TEM) to show that, even after annealing, a Au tip at the terminus of a CdSe NR appears to form an abrupt interface, with "epitaxial" registry of the Au and CdSe nanocrystals (NCs).[24]

In the design of efficient photocatalytic materials, controlling both the average and local energy levels of symmetric or asymmetric NR materials with respect to the catalytic reactions they are intended to accelerate remains a challenge.[2,16,25−29] Measuring these energy levels also presents significant challenges, including: (a) defining E_{VB} and E_{CB} with respect to vacuum scale (and dispersion in these energies), and (b) characterizing the shifts in local vacuum level that may result from metal modification of NRs.[7,30−34] An additional challenge is relating the band energies of heterostructured nanomaterials measured in vacuum to the energetics of these materials in solution/electrolyte media where they are ultimately intended to function.

We previously reported on both UV photoemission (UPS) and spectroelectrochemical characterization of CdSe nanoparticles (NPs) adsorbed or tethered to metal (Au) or metal oxide (indium−tin oxide, ITO) surfaces, to estimate band edge energies.[35,36] UPS was used to estimate E_{VB} for two different populations of monolayer-tethered, ligand-capped CdSe NPs, with diameters of 3.6 and 6 nm, on clean Au substrates, after correcting for shifts in local vacuum level that result from the strong interface dipoles characteristic of these nanomaterials.[36] The use of two different excitation sources, He I (21.2 eV) and He II (40.8 eV), provided two different sampling depths. This work built upon earlier reports by Colvin *et al.*[37] where synchrotron-based photoemission (excitation energy = 20−70 eV) was used to estimate E_{VB} for cadmium sulfide (CdS) NPs tethered to multiple surfaces as a function of NP diameter.

Naaman, Waldeck and co-workers used combinations of photoemission, with low energy excitation sources, and 2-photon photoemission (2PPE) spectroscopy in a complementary fashion to estimate E_{VB} for CdSe NPs, and the effect of ligand type and dipolar nature on band edge energies.[38−40] Jasieniak *et al.* more recently used atmospheric PES on a series of semiconductor NPs (CdSe, CdTe, PbS and PbSe), showing a systematic change in E_{VB} with NP diameter.[34] They estimated E_{CB} using the quasi-particle gap energy (transport gap), which is obtainable *via* the modification of the optical band gap energy with the Coulomb interaction between an electron−hole pair, and the polarization energy arising from carriers and image charges across the high dielectric nanoparticle. For CdSe NPs varying in diameter from *ca*. 2 to 6.5 nm, E_{VB} varied by *ca*. 0.5 eV, while E_{CB} varied by up to 1.0 eV, with both optical and transport band gap energies decreasing with increasing NP diameter, as expected. The corrections to E_{CB} estimated from the optical band gap *vs* the quasi-particle gap energy were up to 0.2 eV depending upon CdSe NP diameter, and were much smaller for this semiconductor than for CdTe, PbS or PbSe.

For various NCs on a variety of contact surfaces, including oxides, estimation of E_{VB} in the high kinetic energy (HKE) region can be problematic due to the large secondary electron scattering coupled with photoemission.[30−32] New approaches to analysis of high kinetic energy UPS data, at E_{VB} and in the midgap region out to the Fermi energy, E_F, as recently demonstrated for molecular semiconductor films,[41,42] now provide more confidence in values of E_{VB} extracted from measurements on NC thin films, and suggest the possibility of probing densities of midgap states that arise from defects in the NCs or, as shown below, the addition of metal tips to a semiconductor NR. For heterostructured NRs, new challenges emerge, since both the core and the tip of the NR are simultaneously sampled in the UPS experiment.

Solution electrochemical methods have been used in a complementary fashion to estimate both E_{VB} and E_{CB} for nanomaterials such as CdSe NPs; however, multilayer films have typically been required, and distinguishing Faradaic currents associated with charge injection/extraction from capacitive currents can be challenging. Significant variations in E_{VB} and E_{CB} using these methods have been observed, which have been attributed to the sensitivity of the electrochemistry of these nanomaterials to surface defects and ligand effects.[36,43−45] Brutchey and co-workers

used voltammetry of multilayer NP thin films to estimate conduction band energies on carefully prepared and purified NPs, to rationalize the effects of NP diameter and ligand type/size on the open-circuit photopotentials of PV platforms created from composites of NPs and a polymer host.[46] They and other groups have shown that the size and charge density of the solution counterion can also significantly alter onset potentials and estimates of E_{VB} and E_{CB}.[33,34,36,46−50]

We recently demonstrated that attenuated total reflectance (ATR) spectroelectrochemistry[51,52] can be used to estimate E_{CB} of submonolayers of CdSe NPs tethered to electroactive (ITO) waveguide surfaces, where the low surface coverages ensure characterization of electron injection events into isolated NPs or small NP clusters.[35] At potentials sufficiently negative to inject electrons into the NP conduction band, the excitonic absorbance band of CdSe is reversibly bleached. Correcting the electrode potential to the vacuum scale provides for an *in situ* estimate of E_{CB}, which in combination with the optically determined band gap, provides for estimation of E_{VB}.[53] Experiments on low surface coverage films may provide somewhat different estimates of E_{CB} relative to transmission spectroelectrochemical experiments of multilayer NC films.[47,54,55]

Herein we report the first use of complementary UPS and spectroelectrochemical measurements of band edge energies, referenced to the vacuum scale, for thin films of CdSe and Au-tipped CdSe NRs (Figure 1). Both approaches show that E_{VB} = 5.9−6.1 eV and E_{CB} = 4.1−4.3 eV for CdSe NRs. In the UPS experiments, the detected photoemission is dominated by the upper surface of the NR film; however, the results are similar to those obtained on control CdSe NPs (*ca.* 2.5 nm diameter) where most of the NP volume contributes to the photoemission signal. We detect significant shifts

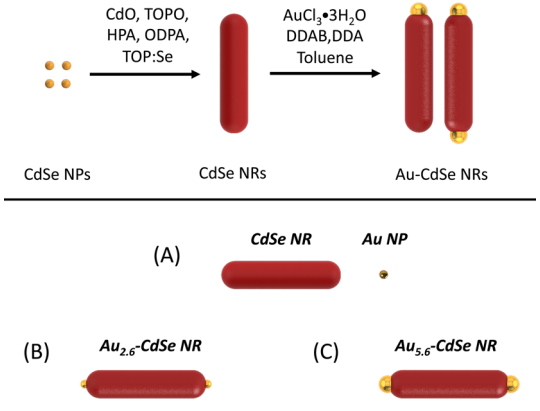

Figure 1. (upper) Synthetic scheme for creation of symmetric and asymmetric Au-tipped CdSe NRs used in this work; (lower) schematic views of (A) the precontact CdSe NR and Au NP, (B) the symmetric $Au_{2.6}$-CdSe NR and (C) the symmetric $Au_{5.6}$-CdSe NR (where the subscript on Au refers to the tip diameter in nm). The Au tips are drawn approximately to scale *vs* the dimensions of the NRs.

in both local vacuum level and E_{VB} as Au tips of increasing size are added to these NRs, and the creation of midgap states (denoted MSI states per Steiner *et al.*[6]) at low densities above E_{VB}. Waveguide-based ATR spectroelectrochemical experiments show that electron injection into the conduction band of CdSe NRs produces bleaching of the lowest energy excitonic features ($1\Sigma_e$ level). For the Au-tipped NRs, additional absorbance changes are observed that are assigned to electron injection into MSI states (as suggested by earlier STS and transient absorbance studies).[1,2,6,20,56] These complementary characterization protocols are likely to be applicable across a variety of new heterogeneous NR materials.

RESULTS AND DISCUSSION

Synthesis of Heterostructured Nanorods. CdSe NRs and Au-tipped CdSe NRs were prepared for these studies using modified literature methods (Figure 1; see Methods for details). CdSe NPs (diameter (D) = 2.7−3.2 nm) were synthesized using previously reported methods[57,58] and used to seed the growth of CdSe NRs (length (L) ≈ 40 nm; D ≈ 9−10 nm) based on a modified literature procedure for CdSe NRs.[57] In our hands, the use of a CdSe seed enabled more precise and reproducible tuning of NR dimensions and uniformity, although the majority of reports on these materials do not require the use of CdSe seeds. Deposition of Au NPs onto NRs was conducted using modified methods of Mokari *et al.*,[5] with $HAuCl_4 \cdot 3H_2O$ as the gold precursor, didodecyldimethylammonium bromide as a surfactant for the gold salt, and dodecylamine as both the reducing agent and stabilizing ligand. This approach afforded a mixture of CdSe NRs with one or two terminal Au NP tips (termed "matchstick" or "dumbbell" tipped NRs, respectively). Representative TEM images are shown in Figure 2.

The size of the Au NP tips was varied by control over the gold precursor and CdSe NR concentrations, allowing for the deposition of tips with diameters ranging from 2 to 6 nm. For the characterization studies

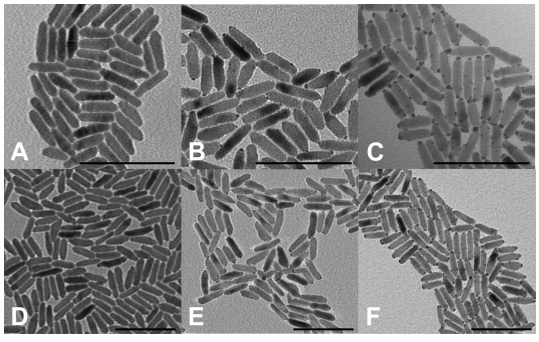

Figure 2. TEM images of (A, D) CdSe NRs (L = 40.1 ± 4.1 nm; D = 9.6 ± 1.2 nm); (B, E) $Au_{2.6}$-CdSe NRs; and (C, F) $Au_{5.6}$-CdSe NRs exhibiting both matchstick and dumbbell morphologies, with a small percentage of the Au NPs deposited along the NR axis as well as at the tips. All scale bars are 100 nm.

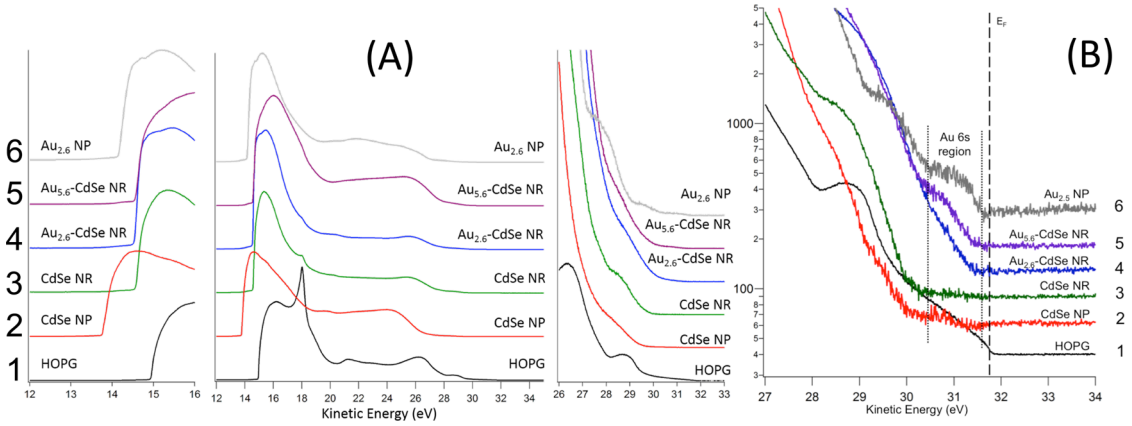

Figure 3. (A) He (I) photoemission spectra of (1) freshly cleaved HOPG, (2) CdSe NPs, (3) CdSe NRs, (4) $Au_{2.6}$-CdSe NRs, (5) $Au_{5.6}$-CdSe NRs and (6) $Au_{2.6}$ NPs, all deposited on freshly cleaved HOPG. Background correction and satellite removal from these spectra and other details of the data analysis procedures are given in SI; (B) The HKE region of the spectra in (A), offset vertically for clarity, corrected for both secondary electron scattering background and satellite photoemission, on a semilog scale to accentuate photoemission from states above E_{VB}, out to E_F, shown here as a dashed line at KE = 31.8 eV. Photoemission from the HOPG substrate is suppressed, and spectral features appear at energies out to E_F due to defects in the NP or NR, or the addition of Au NPs that introduce MSI states (see text).

described below, CdSe NRs were derivatized with two sizes of Au tips, 2.6 and 5.6 nm, denoted as $Au_{2.6}$-CdSe NRs and $Au_{5.6}$-CdSe NRs, respectively. For the smaller tips, a distribution weighted toward singly tipped structures was observed (23.5% untipped, 56.1% singly tipped, and 20.4% with two tips as measured by TEM). For the larger tips, however, the distribution was more heavily weighted to materials with two tips (0.0% untipped, 9.8% singly tipped, and 90.2% with two tips as measured by TEM). Histograms of nanorod tipping distributions are presented in Supporting Information (SI). Although the $Au_{2.6}$-CdSe NRs and $Au_{5.6}$-CdSe NRs tipping distributions were different, the degree of Au metallization of CdSe NRs could be controllably varied, enabling correlation with both UPS and spectroelectrochemical measurements as discussed below.

Photoemission Spectroscopy of Heterostructured Nanorods. UPS was used to estimate E_{VB} for NR monolayers, to characterize low concentrations of midgap states extending out to E_F (introduced by Au tipping), and to characterize variations in local vacuum level as Au tips were added to the NR. CdSe NR or NP films were deposited on freshly cleaved HOPG, as described in SI, producing submonolayer to monolayer coverages. X-ray photoelectron spectroscopy (XPS) was performed on each sample to examine NP or NR composition and stoichiometry (Se/Cd ratio; see SI). Film morphology was assessed using field emission scanning electron microscopy (FE-SEM) (see SI). Low surface coverages were used for these studies because the NR electronic and energetic properties are expected to be more uniform relative to multilayer films.[33,54,55]

UPS data for these NR films are shown in Figure 3, along with reference data for clean HOPG, HOPG coated with a thin film of dodecylamine-capped Au NPs, and HOPG coated with a thin film of small CdSe NPs (2.5 nm diameter; *i.e.*, a diameter which ensures that photoemission from both the surface and the interior of the NP is sampled).[59] The center panel of Figure 3A shows the full photoemission spectra prior to data treatment. The left and right panels show expanded views of the low and high kinetic energy (LKE and HKE) regions, respectively. High sensitivity, log scale presentation of the HKE regions is shown in Figure 3B. For these data we plot the kinetic energy on the *x*-axis and indicate the Fermi energy for the spectrometer/samples (E_F in this case = 31.8 eV), which includes an energy offset from an added voltage applied to the substrate to accelerate photoelectrons to a higher kinetic energy, making their quantification more reliable.[60−62] These kinetic energies are corrected to a binding energy scale for creation of the band energy diagrams in Figure 4A.

In previous experiments using clean Au substrates modified with thiols to adsorb CdS, CdSe and related NPs, we noted the high photoemission background intensity from the substrate and from the thiol linkers themselves,[36,37] whereas for CdSe or PbSe NPs supported on ZnO substrates[30−32] and the HOPG substrates used here, lower secondary electron photoemission background is observed in the critical HKE spectral regions. This secondary emission is suppressed when thin NR or NP films are added to the HOPG surface. The onset of photoemission from the valence band of the NR or NP, along with photoemission from midgap states, if present, is much easier to distinguish with substrates that show only weak photoemission near the HKE region.[63−65] The efficacy of HOPG as a substrate for the determination of valence band photoemission features has been shown to provide more accurate estimates of ionization onset energies for a variety of molecular systems, with fewer concerns about background correction relative to metal substrates such as Au.[66−68]

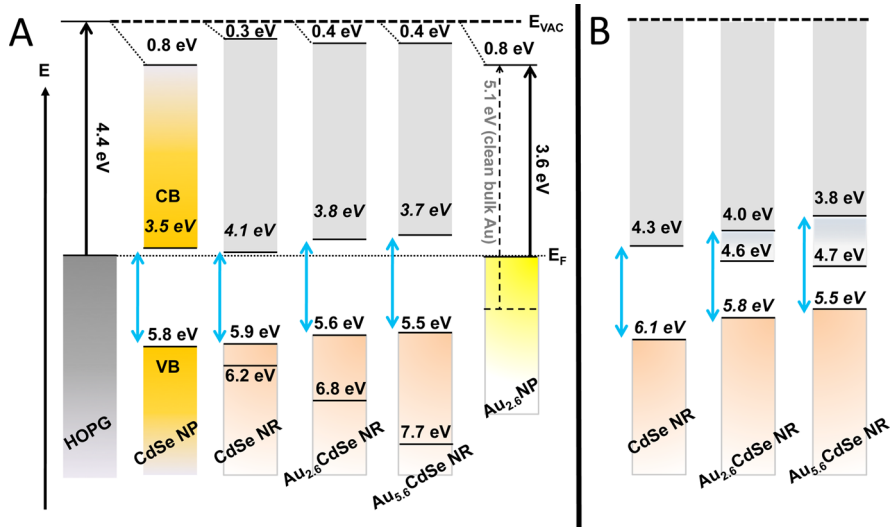

Figure 4. Energetics for CdSe, $Au_{2.6}$-CdSe, and $Au_{5.6}$-CdSe NR films and reference materials. (A) E_{VB} values obtained from the UPS data for NP and NR films on HOPG, corrected for local vacuum level shifts. The E_{VB} shifts closer to vacuum and other ionization features are also observed, much deeper than E_{VB}, as Au tips are added to the NR. E_{CB} values are estimated from E_{VB} values and the optical band gap (blue arrows) for the NP or NR. (B) E_{CB} values for NR films are estimated from the onset potentials for bleaching of the lowest energy band in the difference ATR spectra, which results from electron injection into the $1\Sigma_e$ level of the CdSe NR. The Au-tipped NRs show two "bleaching" transitions: the first is assigned to E_{IS} (due to MSI states in the band gap region with onsets at 4.6 and 4.7 eV for $Au_{2.6}$-CdSe and $Au_{5.6}$-CdSe NR films, respectively) and the second is assigned to E_{CB} (at 4.0 and 3.8 eV for $Au_{2.6}$-CdSe and $Au_{5.6}$-CdSe NR films, respectively). E_{VB} energies are estimated from the optical band gap (blue arrows). As in the UPS experiments, Au tipping moves E_{CB} and E_{VB} closer to vacuum.

The HKE data in Figure 3B have been taken through a series of corrections to enhance the photoemission contribution from the NRs and NPs, since the HKE onset for photoemission above baseline is required to achieve a reliable estimate of E_{VB}. An expanded description of our data treatment is given in SI. We first correct for spectral features arising from He (I) satellite emission in the excitation source (β and γ) at +1.87 and +2.52 eV, relative to the He (I) primary excitation energy (21.2 eV). While these satellite features are low in intensity, and often ignored in normal UPS experiments (and may be missing in PES experiments using monochromatic excitation sources, or in atmospheric photoemission experiments),[31,34,41,42] their presence can make estimates of E_{VB} problematic in some instances. Furthermore, defect states in NRs and other molecular and oxide semiconductors show photoemission that directly overlaps these satellite features, at intensities which are important to the electronic and photocatalytic properties of these materials, but difficult to quantify without satellite removal.

Second, we apply an integrated sigmoidal correction for the contribution to spectral background from the scattering of secondary photoelectrons in the HKE region, as described by Henrich and co-workers,[69] and more recently by Zhu and co-workers,[31] which we find to be more significant for semiconductor nanomaterials than for organic semiconductors. The final correction is a weighted linear subtraction of the remaining background photoemission due to the HOPG substrate, which contributes to the photoemission tail that converges at the Fermi energy and can be seen most clearly in the log−linear representation of the photoemission spectra (shown in SI). If an adequate S/N ratio is achieved, and full correction for satellite photoemission and secondary electron background is performed, it is possible to distinguish differences in E_{VB} energies and work function down to *ca.* ± 0.05 eV.

E_{VB} levels for each NC assembly were next estimated from the difference in the source energy and the energetic width of the photoemission spectrum: E_{VB} = 21.2 eV − [HKE − LKE], after confirming complete removal of satellite peaks and secondary electron scattering background using semilog display (see SI).[60,61,68] This approach provides E_{VB} values (Figure 4A) corrected for local vacuum level shifts.[62] E_{VB} obtained for a control sample, a thin film of CdSe NPs (2.5 nm diameter, optimized capping ligand coverage), is *ca.* 5.8 eV which agrees well with recent reports for CdSe NPs of comparable diameter and capping ligand.[34] A control with a small diameter was chosen to ensure that both the surface and the interior of the NP contributed to the measured photoemission response.

Depending upon excitation energy and the surface-to-volume ratio of the NC, there may be concerns that PES-determined E_{VB} values may be more representative of the near surface region than the bulk of the NC. In our previous studies of CdSe NPs and those of Jasieniak *et al.*, E_{VB} values were measured on a range of NP diameters using different excitation energies which produced different sampling depths.[34,36] For the larger NPs (4−8 nm diameter) probed using the lowest excitation energies, the photoemission signal originated predominately from the near surface regions

(*ca.* 2−3 nm from the NP surface into the interior). When the NP diameter was less than *ca.* 3 nm and/or the excitation energy was high, however, the PES-determined E_{VB} values reflected a larger contribution from the NP interior. Combinations of photoemission with a high energy excitation source and X-ray absorption were used by Meulenberg and co-workers to estimate E_{VB} and E_{CB}, band gap energy, and exciton binding energy in CdSe NPs of varying diameters, which ensured that the bulk of the NP was sampled.[70−72] The comparable values of E_{VB} for both CdSe NPs and NRs from all of these studies suggests that these values are more reflective of intrinsic valence band energies than energies associated with near surface defect states.

The band edge energies of CdSe NRs shift as Au tips are added (Figure 4A). The HKE ionization edge shifts in energy by *ca.* 0.3−0.4 eV; *i.e.*, E_{VB} decreases by up to 0.4 eV relative to the untipped NRs; this shift is discussed further below. Additional higher binding energy features are present in the HKE region for the CdSe NRs (at 6.2 eV in Figure 4A) that shift further from vacuum, to 6.8 and 7.7 eV, for the $Au_{2.6}$-CdSe NRs and $Au_{5.6}$-CdSe NRs, respectively. The physical/chemical origin of these features is not clear and will be a subject of future investigations.

The semilog HKE region above E_{VB} is relatively featureless for the bare CdSe NRs; however, new photoemission features (less than 10% of total photoemission intensity) appear in the band gap as Au tips are added; this is especially apparent for the $Au_{5.6}$-CdSe NRs. Even for the 2.6 nm Au tips, however, we estimate that these features have an energetic full width of *ca.* 0.5 eV and are located at energies close to those predicted for MSI states from STS studies of comparable Au-tipped CdSe NRs.[1,6,73] Interestingly photoemission from these states appears to converge on the features seen for Au 6s states in the photoemission spectra of Au NPs on HOPG, just below E_F, and it is reasonable to expect that, as the Au NP tip increases, we would see photoemission dominated by those portions of the Au tip well away from the CdSe NR/Au NP heterointerface. For both sizes of Au tips, the contribution from these new states extends from E_{VB} out to E_F, suggesting a very heterogeneous energetic environment for these metal-derived states, an observation that is complemented by the spectroelectrochemical results discussed below.

The relatively featureless HKE spectral region above the E_{VB} edge for the bare CdSe NRs enables these observations out to E_F. It should be noted that for more polydisperse CdSe NPs or CdSe NRs with higher defect densities, we observe tailing of the photoemission edge into the middle of the band gap region. The use of our photoemission approach to characterize band edge dispersion in variably sized CdSe NPs and NRs, and the influence of defects on the density-of-state (DOS) distributions of these states, will be reported elsewhere.

E_{CB} levels for CdSe NPs, CdSe, $Au_{2.6}$-CdSe, and $Au_{5.6}$-CdSe NR films were then estimated by adding the optical band gap, E_{opt}, to E_{VB}. E_{opt} values were estimated from the low energy onset of the lowest energy absorbance band (shown in SI; Figure S5). For CdSe NPs, E_{opt} = 2.31 eV which yielded E_{CB} = −3.2 eV *vs* vacuum. For CdSe, $Au_{2.6}$-CdSe, and $Au_{5.6}$-CdSe NRs, the respective E_{opt} values were 1.78, 1.78, and 1.75 eV. Since there was no significant difference among these values and the E_{VB} estimates have an associated error of ±0.05 eV, E_{opt} = 1.8 eV was used to estimate the E_{CB} levels for NRs shown in Figure 4A. As shown by Meulenberg and co-workers and Jaseniak *et al.*, these E_{opt} values may be smaller than the "photoelectron gap" determined from combinations of PES and XAS; however, for the diameter of the NRs studied here, these differences are likely to be well under 0.2 eV.[34,70−72]

As has been discussed extensively for other complex organic and inorganic semiconductor/contact heterojunctions, changes in effective work function, $\Delta\phi$, are expected for all HOPG/NR or HOPG/NP heterojunctions as they achieve electronic equilibrium (Fermi levels aligned with that of the spectrometer), and the sign and magnitude of these changes are determined by the precontact work functions of the individual components of the heterojunctions.[60−62] Estimates of ϕ were obtained from ϕ = 21.2 eV − [E_F − LKE], where E_F is the Fermi energy of the sample and spectrometer (dashed line, right side of Figure 3B). The addition of CdSe NPs or NRs decreases ϕ relative to the HOPG substrate, consistent with addition of a strongly dipolar layer to the HOPG surface (positive end of the dipole pointed toward vacuum) as a result of electronic equilibration.[62] For CdSe NP thin films, there is a substantial vacuum level shift (*ca.* 0.8 eV), whereas for the CdSe NR films the vacuum level shift relative to clean HOPG is smaller, but still produces a lower ϕ (see Figure 4A). These data suggest that the CdSe NPs and CdSe NRs are *n*-type semiconductors with a precontact work function lower than that of bare HOPG,[62] with E_F within *ca.* 0.3 eV (or less) of the estimated E_{CB}. The observation of a Fermi energy this close to the estimated E_{CB} suggests that, in the upper region of the NP and NR films (the sampling depth is less than *ca.* 3 nm for 21.2 eV excitation), these materials are rich in electron-donating sites (defects) which is consistent with the XPS-derived Se/Cd ratios that are below stoichiometric values for both the NPs and NRs (see XPS data in SI). The role that these defect states play in achieving electronic equilibrium with the HOPG substrate is under investigation.

Addition of Au tips results in an E_F closer to the middle of the band gap region, as expected if electron transfer from the CdSe NR to an intrinsically higher

work function Au tip takes place. However, the direction of charge flow as the Au tip equilibrates with the NR is difficult to predict. As depicted in SI (Figure S14), at an *isolated* Au/CdSe heterojunction, an increase *or* decrease in local vacuum level might occur, depending upon the precontact work function of the Au NP, which in these studies is not well understood. For clean (bulk) Au, $\phi \approx 5.1$ eV (shown schematically in Figure 4A).[60,61] In contrast, recent studies of work functions for Au NPs have shown that, for small particle diameters, the effective work function can be substantially lower,[74] which is consistent with our measurement of $\phi = 3.6$ eV for Au NP thin films (Figure 4A). If the work function of the Au NP is lower than that of the bare CdSe NR (4.1 eV), then electron transfer from the Au tip to the CdSe NR would occur upon equilibration. This case is consistent with the measured shifts in E_{VB} toward vacuum (Figure 4A) that indicate that Au tipping increases the electron density in the NR. Furthermore, when considering the measured changes in E_{VB} and ϕ, it important to note that the Au tips are small with respect to the overall length of the NR (see Figures 1 and 2), and photoemission must be dominated by the upper surface of the CdSe core of the NR, well removed from the Au/CdSe heterojunctions at one or both termini. Thus, the measured $\Delta\phi$, averaged over the entire NR upper surface, is expected to be less than the local change at/near the Au/CdSe heterojunctions. In summary, these Au-tipped NR films are significantly more complex assemblies than previously characterized planar heterojunctions, which are relatively uniform in composition; however, the changes in band edge energies that we observe are entirely consistent with those observed in our spectroelectrochemical studies (see below).

Finally, we also considered whether the ligands (didodecylamine and dididodecyldimethylammonium bromide) introduced during Au tipping of CdSe NRs, which are different from those used for CdSe NR synthesis, might be responsible for the measured changes in E_{VB}. A ligand exchange reaction was performed on CdSe NRs in conditions identical to the process used to produce 2.6 nm Au tips, except the Au(III)Cl precursor was absent. The resulting local vacuum level was 0.6 eV lower than that of HOPG, and E_{VB} was −5.8 eV; *i.e.*, the measured E_{VB} and vacuum level shifts are within experimental error of the values measured for CdSe NRs not subjected to ligand exchange. This result also shows that the Au tipping process did not alter (*e.g.*, etch) the NR structure to a degree that would cause a change in energetics.[5]

Spectroelectrochemical Characterization of Heterostructured Nanorods. Potential-controlled, visible ATR spectroscopy was performed using ITO-coated glass as the planar waveguide and working electrode, to provide estimates of E_{CB} for NR films. Details of the instrumentation and procedures are given in SI and in previous publications.[35,75] Briefly, bare ITO electrodes were first treated with 1,8-octanediphosphonic acid (OdiPA), prior to spin coating of NR solutions, to ensure robust tethering and sufficient coverage of NRs on these electrodes. NR-modified ITO substrates were then soaked in ethanol for 1 h before characterization experiments were performed. This step improved the electrochemical response, presumably by removing unbound ligands and promoting NR adhesion to the OdiPA modifier. Deposition conditions were identified that produced uniform low coverages (from near monolayer for CdSe NRs and $Au_{2.6}$-CdSe NRs to 1−2 monolayers for $Au_{5.6}$-CdSe NRs), as verified by FE-SEM (see SI).

ATR spectra of NR films immersed in 0.4 M $LiClO_4$ in degassed acetonitrile were acquired as a function of the potential applied to the ITO with respect to a $Ag/AgNO_3$ pseudoreference electrode. As the potential was stepped to more negative values, progressive bleaching of the NR absorbance features was observed. These bleaching events correlate with Faradaic (electron injection) processes that are detected without interference from background charging currents inherent in conventional electrochemical measurements.[33,54,76,77] For this reason, optical probes of electron injection into low surface coverage NR films are far superior to conventional electrochemical probes.[35] For all three types of NR films, the wavelength maxima of the bleaching bands in the ATR difference spectra (presented below) correspond well with the positions of the major bands in the absorbance spectra of dissolved NRs (see SI, Section 3). Furthermore, the bleaching was *ca.* 100% reversible for all three types of NR films when the potential was stepped back to the prebleach value, provided that potentials more negative than *ca.* −1.25 V were not applied. When potentials more negative than *ca.* −1.25 V were applied, the reversibility was *ca.* 90−95% (see ATR difference spectra presented below). Less than complete reversibility is attributed in part to irreversible reduction of ITO, which has an onset near −1.25 V.

Spectroelectrochemistry of CdSe NRs. Representative ATR difference spectra of CdSe NRs on ITO, referenced to the spectrum measured at −0.45 V, are plotted in Figure 5A. At potentials more negative than −0.75 V, a bleaching band appeared with $\lambda_{max} \approx$ 680 nm. At potentials negative of *ca.* −1.00 V, this band broadened to higher energies with λ_{max} closer to 670 nm. A less intense bleaching band with $\lambda_{max} \approx$ 555 nm also appeared at potentials more negative than −0.75 V and, similar to the lower energy band, it broadened at potentials negative of *ca.* −1.00 V. The presence of more than one optical transition in each of these bands can be attributed to compositional heterogeneity and/or energetic heterogeneity. The uniformity of the untipped NRs in the images in Figure 2 and in SI suggests that energetic heterogeneity in otherwise uniform NRs, *i.e.*, charge injection to

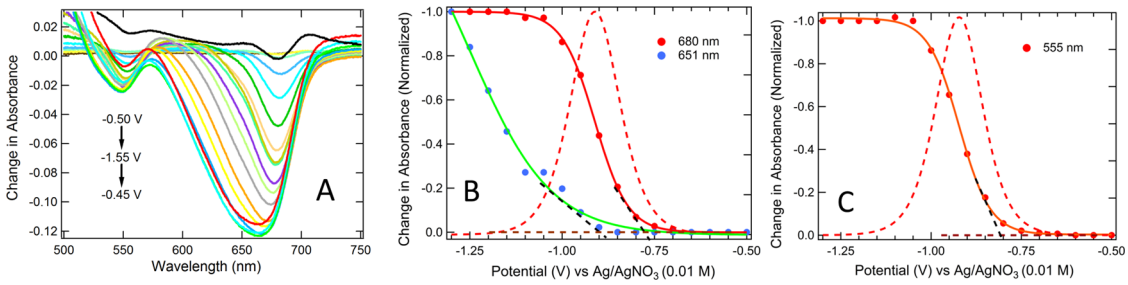

Figure 5. (A) A representative set of potential-controlled ATR difference spectra of CdSe NRs tethered to OdiPA-modified ITO. Spectra were acquired at intervals of 0.05 V from −0.50 V to −1.55 V and normalized to the spectrum acquired at −0.45 V. The plotted spectra cover the range of −0.70 V to −1.55 V. Bleaching of absorbance bands at *ca.* 680, 651, 555, and 534 nm was observed. The black curve is the spectrum measured when the potential was stepped back to −0.50 V, which shows the degree of reversible bleaching. The wavelength maxima were obtained by fitting the difference spectra to a model composed of Gaussian bands (two bands at > −1.15 V; four bands at ≤ −1.15 V; see example in SI). (B, C) Difference absorbance (normalized) plotted as a function of potential at 680 nm, 651 nm (B), and (C) 555 nm. Solid lines are sigmoidal fits. The black dashed lines are extrapolations drawn to estimate the onset potentials for these transitions. The red dashed curves are first derivative plots of difference absorbance *vs* potential at 680 and 555 nm.

different quantum confined states, as first observed by Guyot-Sionnest and co-workers for CdSe NCs,[54] is the more likely explanation.

To determine the number of absorbance transitions and their respective spectral profiles (peak wavelength, fwhm, and intensity), each difference spectrum in Figure 5A was fit with Gaussian components (see example in SI; Figure S12). This analysis showed that at potentials positive of *ca.* −1.15 V, the difference absorbance band in the 590−730 nm region is composed of one band with $\lambda_{max} \approx 680$ nm, whereas at potentials negative of *ca.* −1.15 V, a second band with $\lambda_{max} \approx$ 651 nm is present. Likewise, the difference absorbance band in the 500−590 nm region was fit with a single Gaussian component with $\lambda_{max} \approx 555$ nm at potentials > *ca.* −1.15 V; at potentials < *ca.* −1.15 V, a second, minor component appeared with $\lambda_{max} \approx 534$ nm.

These absorbance features of CdSe NRs, assumed to arise from 1D excitons, are assigned based on the work of Efros and co-workers.[78] In Figures 5B and 5C, the difference absorbance at the λ_{max} for the three major bands is plotted, along with sigmoidal fits to the data. The apparent onset potential for bleaching at each λ_{max} was obtained by extrapolating the slope of each sigmoidal curve to the asymptote corresponding to the neutral CdSe NR film (dashed lines). The bands at 680 and 555 nm begin to bleach at onset potentials of -0.77 ± 0.01 V and -0.80 ± 0.33 V ($n = 4$), respectively, showing that these transitions are correlated. We posit that bleaching of these bands is due to electron injection into the $1\Sigma_e$ level of the CdSe NR conduction band. The onset potential for bleaching of the 651 nm band occurs at *ca.* -0.93 ± 0.05 V, and is assigned to electron injection into the $1\Pi_e$ level of the CdSe NR conduction band. The difference between the onset potentials for the 680 and 651 nm bleaching transitions, 0.16 V, is the $1\Sigma_e - 1\Pi_e$ intraband energy.[79]

The midpoint potentials for bleaching of the 555 and 680 nm bands were obtained by computing the first derivative of the sigmoidal fits to the bleaching data. Figure 5B shows the plot for the 680 band; the dashed line assigns the midpoint potential for injection into the $1\Sigma_e$ level which is -0.93 ± 0.06 V. The same midpoint potential, -0.92 ± 0.06 V, was obtained for the 555 nm band (Figure 5C). The midpoint potential could not be determined accurately for the 651 nm band because the bleaching was incomplete at −1.55 V, beyond which irreversible reduction of ITO significantly distorted the difference spectra.

To estimate the onset E_{CB} for CdSe NR films, the onset reduction potential was corrected to the vacuum scale using a value of −4.48 eV *vs* vacuum for the potential of the normal hydrogen electrode (NHE).[53] The midpoint potential of the ferrocene/ferricenium (Fc/Fc^+) redox couple used to calibrate the $Ag/AgNO_3$ (0.01M) reference electrode was 0.07 V. The potential of Fc/Fc^+ was taken to be 0.64 V *vs* NHE,[80] and E_{CB} was therefore estimated from $E_{CB} = -(E_{red} + 5.05)$ eV, where E_{red} is the onset reduction potential *vs* $Ag/AgNO_3$, which was −0.77 V for the 680 nm bleaching band. This treatment yielded an onset E_{CB} of -4.28 ± 0.01 eV for the $1\Sigma_e$ level. The onset E_{VB}, −6.06 eV, was estimated by subtracting the optical band gap (E_{opt} = 1.78 eV). These band energies are plotted in Figure 4B.

Spectroelectrochemistry of Au-Tipped CdSe NRs. The spectroelectrochemical properties of Au-tipped CdSe NRs showed absorbance changes *vs* potential over a broader potential range than for the untipped NRs. Changes in absorbance of the $Au_{2.6}$-CdSe NR films began as the potential was stepped negative of −0.35 V; the ATR difference spectra plotted in Figure 6A were therefore referenced to the spectrum measured at 0.0 V. The spectra were fit with two Gaussian bands in the 600−700 nm region, with $\lambda_{max} \approx 682$ nm and $\lambda_{max} \approx 650$ nm. Bleaching also was observed at *ca.* 555 nm but the S/N of the spectra was too low to permit quantitative analysis.

In Figure 6B, the difference absorbance data at 681 and 650 nm show that bleaching occurred over a wider

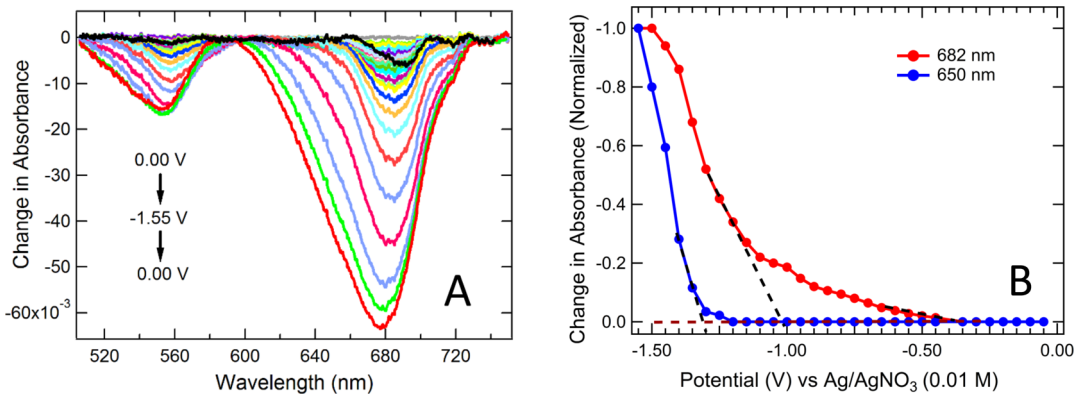

Figure 6. (A) A representative set of potential-controlled ATR difference spectra of $Au_{2.6}$-CdSe NRs on OdiPA-modified ITO. Spectra were acquired at intervals of 0.05 V over the range of 0.00 V to −1.55 V at intervals of 0.05 V and ratioed to the spectrum acquired at 0.00 V. The plotted spectra cover the range of −0.50 V to −1.55 V. For clarity of presentation, some spectra were offset to compensate for potential-dependent shifts in the background. Bleaching peaks were observed at *ca.* 682 and 650 nm. The black curve is the spectrum measured when the potential was stepped back to 0.00 V, which shows the degree of reversible bleaching. The wavelength maxima were obtained by fitting the difference spectra to a model composed of Gaussian bands. (B) Difference absorbance (normalized) as a function of potential at 682 and 650 nm and plotted from the spectral data shown in (A). The solid red and blue lines are drawn to aid the eye in connecting the data points. The black dashed lines are extrapolations drawn to estimate the onset potentials for the transitions.

potential range *vs* bare CdSe NRs, and the 681 nm plot could not be fit to a single sigmoidal function; it contains two nearly linear regions which is indicative of two distinct bleaching processes. Onset potentials for each region were therefore estimated by extrapolation to the asymptote corresponding to the neutral NR film, from which values of −0.48 ± 0.03 V and −1.06 ± 0.04 V (n = 3) were obtained, denoted respectively as E_{red2} and E_{red1}. An onset potential of −1.32 ± 0.03 V (n = 3) for 650 nm bleaching curve, which is assigned to the $1\Pi_e$ transition, was also estimated by extrapolation to the asymptote corresponding to the neutral NR film. (Note: midpoint potentials for these transitions were not determined because the absorbance changes were incomplete at −1.55 V and/or the curves could not be fit to a single sigmoidal function. This was true for all Au-tipped NR samples.) Two onset energies, denoted E_{IS} and E_{CB}, were estimated from E_{red2} and E_{red1} using the procedure described above, yielding values of −4.57 ± 0.03 eV and −3.99 ± 0.04 eV, respectively (Figure 4). E_{CB} is assigned as the conduction band edge ($1\Sigma_e$ transition) and E_{IS} is posited to result from electron injection into MSI states (see below).[1,6,73] Subtracting E_{opt} = 1.78 eV from E_{CB} yielded −5.77 eV for the onset E_{VB}. These band energies are plotted in Figure 4B.

Control experiments were performed to determine if changes in ligand structure and ligand coverage that may have occurred during the Au tipping reaction affected band energies, as was discussed above for UPS experiments. A ligand exchange reaction was performed on CdSe NRs that was identical to the process used to introduce 2.6 nm Au tips, except the Au(III)Cl precursor was absent. Bleaching of the 680 nm band was fit to a single sigmoidal function with an onset potential of −0.73 ± 0.01 V, consistent with the results measured for CdSe NRs that were not subjected to ligand exchange. Therefore, the observation of two distinct bleaching processes cannot be attributed to changes in the NR as a result of ligand exchange.

ATR difference spectra showing the bleaching of the $Au_{5.6}$-CdSe NR films as a function of applied potential are presented in Figure 7A. The behavior was qualitatively similar to that of the $Au_{2.6}$-CdSe NR films; however, some important differences were observed: (a) The spectra in the 600−700 nm region were adequately fit with only one Gaussian band with $\lambda_{max} \approx$ 686 nm. Bleaching in the 550−560 nm region was too minor to accurately quantitate. These differences are attributable to the bleaching depth and S/N of these spectra, both of which were less than that of the CdSe and $Au_{2.6}$-CdSe NR films. (b) The difference absorbance data at 686 nm, plotted in Figure 7B, show that bleaching occurred over a wider potential range compared to both CdSe and $Au_{2.6}$-CdSe NR films. Similar to the $Au_{2.6}$-CdSe NR data, the curve contains two distinct regions indicative of two bleaching processes. Onset potentials for each region were estimated as described above, from which values of −0.39 ± 0.03 V and −1.25 ± 0.15 V (n = 4) were obtained for E_{red2} and E_{red1}, respectively. In comparison to the $Au_{2.6}$-CdSe NR results, the bleaching process denoted by E_{red2} accounted for a noticeably larger fraction of the total bleaching. (c) Two onset energies, E_{IS} and E_{CB}, were estimated using the procedure described above, yielding values of −4.66 ± 0.03 eV and −3.80 ± 0.15 eV that are assigned to MSI states and the conduction band edge (the $1\Sigma_e$ transition), respectively. Subtracting E_{opt} = 1.75 eV from E_{CB} yielded −5.54 eV for the onset E_{VB} level. These band energies are plotted in Figure 4B.

The assignment of the bleaching transitions shown in Figures 6 and 7 to electron injection into MSI states

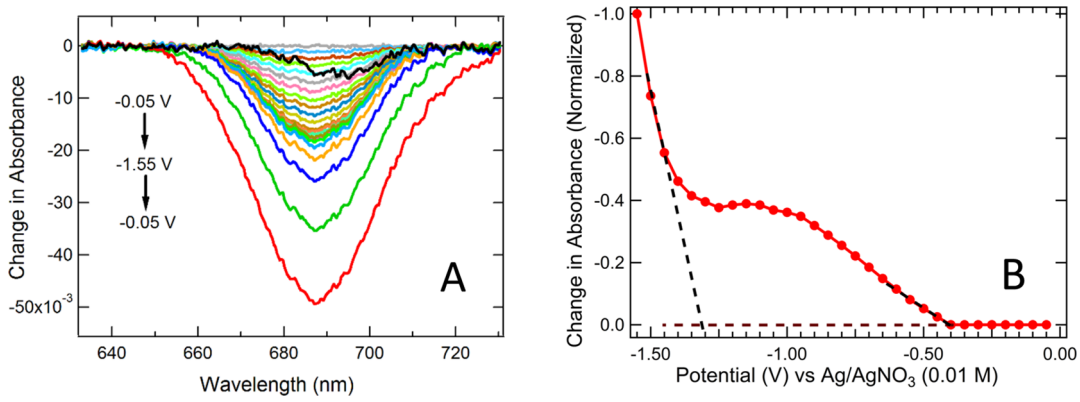

Figure 7. (A) A representative set of potential-controlled ATR difference spectra of $Au_{5.6}$-CdSe NRs on OdiPA-modified ITO. Spectra were acquired at over a potential range of −0.05 V to −1.50 at 0.05 V increments and ratioed to the spectrum acquired at 0.00 V. The plotted spectra cover the range of −0.45 to −1.55 V. For presentation, some spectra were offset to compensate for potential-dependent shifts in the background. Bleaching was observed with a peak wavelength of 686 nm. The black curve is the spectrum measured when the potential was stepped back to −0.05 V, which shows the degree of reversible bleaching. (B) Difference absorbance (normalized) as a function of potential at 686 nm and plotted from the spectral data shown in (A). The solid red line was drawn to aid the eye in connecting the data points. The black dashed lines are extrapolations drawn to estimate the onset potentials for two bleaching processes.

(E_{IS}) and the conduction band edge (E_{CB}) are consistent with the STS studies of Millo, Banin and co-workers.[6,23] Measurements made near the center of Au-tipped rods produced tunneling spectra with an energy gap of *ca*. 2 eV, corresponding to the CdSe band gap region, flanked by numerous conduction and valence band states. Measurements made in the vicinity of a Au tip revealed the presence of MSI states within the energy gap, as well as single electron tunneling (SET) features corresponding to the Coulomb staircase characteristic of Au NPs.[6,81] Also relevant are the reports by Costi *et al.*,[1,2] which indicate that multiple electrons can be injected into a single Au-tipped NR. Unlike STS, the spectroelectrochemical experiments described herein address *ensembles* of Au-tipped NRs. As the ITO electrode potential is scanned to more negative potentials (closer to vacuum), electrons are injected into an ensemble of electrochemically active states, including SET levels, MSI states, and CdSe conduction band states. Injection into the SET and MSI levels will occur at less negative potentials, followed by injection into the CdSe conduction band at more negative potentials.[6] (Note: this process requires electrochemical coupling between the Au NP tips and the ITO surface; further experimental evidence supporting Au-ITO coupling is provided by the potential modulated-ATR results presented in SI). Since injection into the SET levels of the Au tip is unlikely to cause bleaching of the NR absorbance, the SET features observed by STS are unlikely to be detectable by spectroelectrochemistry. However, if the MSI states are electronically coupled to the NR conduction band (*i.e.*, tunneling occurs between MSI states and the conduction band),[6,81] then injection into the MSI states will contribute to bleaching of the lowest energy NR absorbance. We therefore posit that bleaching transitions of Au-tipped NRs having an onset near −4.6 eV are due to charge injection into MSI states.

Comparing Figures 6B and 7B, it appears that the energy distribution of MSI states broadens as the size of the Au tip is increased from 2.6 to 5.6 nm, which is indicated by comparing $|E_{CB} - E_{IS}|$ for $Au_{2.6}$-CdSe NRs (0.58 V) and $Au_{5.6}$-CdSe NRs (0.86 V). In addition, the E_{IS} bleaching process accounts for a considerably larger fraction of the total bleaching of $Au_{5.6}$-CdSe NR absorbance relative to that of $Au_{2.6}$-CdSe NR absorbance. These observations suggest that the introduction of the 5.6 nm tip creates a greater density of MSI states having a broader energy distribution.

Comparison of UPS and Spectroelectrochemical Approaches for Estimating Energetics of Heterostructured Nanorods. To our knowledge, the data presented in Figure 4 represent the first attempt to correlate measurements of E_{VB}, obtained from photoemission experiments, with measurements of E_{CB} obtained from electrochemical or spectroelectrochemical measurements, for nanorod semiconductors. Both the UPS results and the spectroelectrochemcial results show that for untipped CdSe NRs, E_{VB} = 5.9−6.1 eV and E_{CB} = 4.1−4.3 eV. Both approaches show that Au tipping of CdSe NRs produces significant changes: (a) E_{VB} and E_{CB} levels are shifted closer to vacuum, by about 0.3 eV for $Au_{2.6}$-CdSe NRs and about 0.4−0.6 eV for $Au_{5.6}$-CdSe NRs. (b) Midgap electron injection processes (MSI states) are introduced, with spectroelectrochemically detected onset energies (E_{IS}) near −4.6 eV. Apparently complementary states above E_{VB} are detected in the photoemission experiments, and are also assigned as MSI states. Local vacuum level shifts that might allow prediction of charge flow during electronic equilibration of the Au tip with the NR are quite small, although the E_{VB} and E_{CB} shifts suggest that this process involves electron transfer from a lower work function Au NP into the CdSe NR (see SI, Figure S14).

The UPS and spectroelectrochemical determinations of E_{VB} and E_{CB} are in good agreement despite

significant differences between the physical basis of these methods and their sampling geometries: (a) Photoemission is detected from the uppermost 1−3 nm of the NR film.[36,60−62] Since the NR diameter is *ca.* 9 nm, the measured E_{VB} energies, and the shifts in E_F relative to E_{VB} and E_{CB} due to charge exchange between the Au tip and the CdSe NR, primarily reflect the properties of the upper third of the horizontally arranged NRs on the HOPG substrate. In the waveguide ATR geometry, the entire NR film thickness is optically interrogated because the penetration depth of the evanescent field[82] is much greater than the rod diameter. When the waveguide is used as a working electrode, the electroactive portion of the film is optically interrogated; thus the shifts in E_{CB} and the introduction of MSI states below E_{CB} due to Au tipping reflect energetic changes in NRs that are electrochemically coupled to the ITO electrode. (b) UPS measurements are made in vacuum, whereas spectroelectrochemistry is performed in relatively high concentrations of electrolytes, and both the solvent and the electrolyte may significantly affect the measured E_{CB}. For example, Boehme *et al.*[33] recently showed that differences in the size of the supporting electrolyte cation can produce shifts in the electrochemically determined E_{CB} of CdSe NPs of up to 0.5 eV. (c) UPS measurements are corrected for local shifts in the vacuum level that can be attributed to a change in the local dipole in the photoemission sampling region, averaged over the length of the NR.[36,60−62] Spectroelectrochemical data are not corrected for local vacuum shifts; it is assumed that the working and reference electrodes are at the same local vacuum level and that any local dipolar fields are compensated in high ionic strength electrolyte environments. (d) Previous studies have indicated that Au tipping allows for accumulation of multiple negative charges on a single NR,[1,2] and the charge capacity per NR should increase as the size of the Au tip increases. We hypothesize that as the potential of the ITO electrode is scanned negative (toward vacuum), filling the lower energy SET and MSI levels in an Au-tipped NR, Coulombic repulsion makes it thermodynamically less favorable for additional electron injection. A larger overpotential may therefore be required for injection into the conduction band, which will be manifested as an apparent shift in E_{CB} closer to vacuum. In summary, although the trends in E_{VB} and E_{CB} values measured for a series of NRs using UPS and spectrolectrochemistry are expected to be similar, the significant differences in these approaches make it possible that the respective E_{VB} and E_{CB} values will differ systematically. Band edge energies of semiconductor NCs, especially heterostructured nanomaterials, should therefore be characterized utilizing more than one measurement approach.

CONCLUSIONS

The band edge energies of heterostructured NRs directly affect the efficiency of these materials as catalysts for photoelectrochemical charge transfer reactions, *e.g.*, the formation of H_2 from protic solvents; thus it is clear that E_{CB} and E_{VB} must be characterized quantitatively as a function of NR structure and composition, ligand composition, solvent/electrolyte system, *etc.* To our knowledge, the UPS and spectroelectrochemical data described herein provide the first quantitative description of the effects of Au NP addition to CdSe NRs on E_{CB} and E_{VB}, referenced to the vacuum scale. The results provide considerable insight into the electronic structure of these heterostructured nanomaterials. UPS with improved background correction procedures provides better estimates of E_{VB} and local vacuum shifts as a function of NR composition and structure, and waveguide spectroelectrochemistry provides the sensitivity required to measure E_{CB} of submonolayer NR films. For untipped CdSe NRs, both approaches show $E_{VB} = 6.0 \pm 0.1$ eV and $E_{CB} = 4.2 \pm 0.1$ eV. Upon Au tipping, shifts in the local vacuum level and in E_{VB} toward vacuum were observed by UPS, as well as the introduction of midgap states. The spectroelectrochemical results show shifts in E_{CB} upon Au tipping, similar to the UPS results; they also reveal that MSI states are generated and indicate that their energy distribution is dependent on the size of the Au NP. The combination of UPS and spectroelectrochemical methods is a powerful approach for studying of structure−property relationships of heterostructured NRs, and can be applied to a wide variety of other types of nanomaterial-based catalysts for photoelectrochemical reactions.

MATERIALS AND METHODS

NC Synthesis: Materials and Instrumentation. All chemicals were used as purchased. Anhydrous 1,2-dichlorobenzene (DCB) (99.9%), 1-octadecene (ODE) (90%), toluene (99.5%), cadmium(II) oxide (99.5%), selenium (99.999%), didodecyldimethylammonium bromide (DDAB) (98%), dodecylamine (DDA) (98%), and gold(III) chloride trihydrate (99.9%) were purchased from Aldrich. Octadecylphosphonic acid (ODPA) (97%), trioctylphosphine oxide (TOPO) (99%), trioctylphosphine (TOP) (90%), trioctylphosphine (TOP) (97%), and hexylphosphonic acid (HPA) (97%) were purchased from Strem. Absolute ethanol was commercially available from Pharmco-Aaper and used as received. An Omega temperature controller CSC32K with a K-type utility thermocouple and a Glas-Col fabric heating mantle were used for CdSe NP synthesis, CdSe NR synthesis, and Au-CdSe NR synthesis. All centrifugation was performed in 50 mL centrifuge tubes using a rotor with a radius of 11 cm. TEM images were obtained on a Tecnai G2 Spirit transmission electron microscope at 80 kV, using carbon-coated copper grids (Cu, square, 200 mesh) purchased from Electron Microscopy Sciences. Image analysis was performed using ImageJ software (Rasband, W.S., National Institutes of Health, http://rsb.info.nih.gov/ij/, 1997-2007). TGA analysis was carried out using a TGA Q50 (TA Instruments) instrument and software from TA Instruments. UV−vis spectra were

obtained using a Model 440 UV−vis Spectrophotometer (S.I. Photonics). Fluorescence measurements were obtained using a FL3−11 Fluorolog-3 Spectrofluorometer (Jobin Yvon-Spex Instruments SA).

CdSe NP Synthesis. *a. Preparation of TOP:Se Stock Solution for CdSe NPs.* To a 20 mL glass scintillation vial equipped with a 1/2″ Teflon coated stir bar was added 1.34 g (1.70×10^{-2} mol) of elemental Se. The vial was sealed with a rubber septum, pumped to a vacuum for 10 min, and subsequently backfilled with Ar. The evacuating and backfilling process was repeated two times. TOP (97%, 10.0 mL, 8.31 g, 2.24×10^{-2} mol) was then injected under argon and the mixture was stirred/sonicated until clear and homogeneous.

b. Synthesis of CdSe NPs on a 600 mg Scale (Relative to CdO). The synthesis of CdSe NPs was adapted from the literature.[57] To a 250 mL three-neck-round-bottom flask equipped with a reflux condenser and 1″ glass coated stir bar, TOPO (30.0 g, 7.76×10^{-2} mol), ODPA (2.80 g, 8.37×10^{-3} mol) and CdO (0.600 g, 4.67×10^{-3} mol) were added. The contents of the flask were then heated to 150 °C *in vacuo* for 30 min with continuous stirring (300 rpm) using a heating mantle and temperature probe to remove any adventitious moisture and air from the vessel. The red, heterogeneous mixture was subsequently heated to 300 °C under Ar to dissolve the CdO until an optically clear and colorless solution had formed. At this point, TOP (90%, 18.0 mL, 15.0 g, 4.05×10^{-2} mol) was injected into the flask and the temperature was then allowed to recover to 380 °C. Upon reaching 380 °C, the heating mantle was removed and the temperature was allowed to decrease to 370 °C. At 370 °C, the TOP:Se stock solution was injected (4.0 mL; described above). After 13 s, 40 mL of ODE was injected into the flask over 10 s in order to facilitate rapid cooling. Room temperature toluene (20 mL) was injected into the flask upon cooling to 110 °C to prevent solidification of the low melting point solid in the reaction mixture (TOPO). The red, homogeneous product was then purified as described below.

Purification involved three centrifugation steps using 50 mL centrifuge tubes. The room temperature product was evenly distributed between six centrifuge tubes, each of which was then diluted to 25 mL with toluene, and precipitated by the addition of 20 mL of ethanol. The mixture was then subjected to centrifugation at 9000 rpm for 7 min, which yielded yellow tinted supernatants and red-orange pellets. The supernatants were then decanted and the pellets were dispersed in 20 mL of toluene before addition of 25 mL of ethanol to each. The mixture was then subjected to centrifugation at 9000 rpm for 7 min, which yielded clear supernatants and red-orange pellets. The supernatants were then decanted and the pellets were dispersed a final time in 20 mL of toluene before addition of 25 mL of ethanol to each. The mixture was then subjected to centrifugation at 9000 rpm for 7 min, which yielded clear supernatants and red-orange pellets. After the final centrifugation step, the red-orange pellets were dried *in vacuo* at 55 °C overnight to yield 1.274 g (59.23 wt % organics by TGA) of a red-orange solid. UV−vis spectroscopy indicated that the CdSe NPs exhibited an average diameter of 2.5 nm (λ_{max} = 512 nm) as indicated by the low energy absorbance peak method of Peng *et al.*[83]

CdSe NR Synthesis. *a. Preparation of TOP:Se Stock Solution for 40.1 × 9.6 nm CdSe NRs.* To a 20 mL glass scintillation vial equipped with a 1/2″ Teflon coated stir bar was added 62.6 mg CdSe NPs (2.5 nm; 59.23 wt % organic content by TGA) and 0.820 g (1.04×10^{-2} mol) elemental Se. The vial was sealed with a rubber septum, pumped to vacuum for 10 min, and subsequently backfilled with Ar. The evacuating and backfilling process was repeated two additional times. TOP (97%, 10.0 mL, 8.31 g, 2.24×10^{-2} mol) was then injected under argon and the mixture was stirred/sonicated until clear and homogeneous.

b. Synthesis of 40.1 nm × 9.6 nm CdSe NRs. The synthesis of CdSe NRs was adapted from the literature.[57] To a 100 mL three-neck-round-bottom flask equipped with a reflux condenser and 1″ glass coated stir bar, TOPO (15.0 g, 3.88×10^{-2} mol), ODPA (1.45 g, 4.34×10^{-3} mol), HPA (1.60 g, 9.63×10^{-3} mol), and CdO (0.750 g, 5.84×10^{-3} mol) were added. The contents of the flask were then heated to 150 °C *in vacuo* for 30 min with continuous stirring (300 rpm) using a heating mantle and temperature probe to remove any adventitious moisture and air. The red, heterogeneous mixture was subsequently heated to 300 °C under Ar to dissolve the CdO until an optically clear and colorless solution formed. At this point, TOP (97%, 9.0 mL, 7.5 g, 2.0×10^{-2} mol) was injected into the flask and the temperature was allowed to recover to 370 °C. The temperature was held at 370 °C for 30 min prior to injection of the stock solution; for the first 20 min, the vessel was wrapped in aluminum foil, and for the final 10 min prior to injection, the vessel was wrapped in cotton in order to facilitate quick temperature recovery after stock solution injection. The CdSe NP/TOP:Se stock solution (9.0 mL; described above) was then quickly injected into the flask and the nanocrystals were allowed to grow for 3 min before the heating mantle and cotton wrap were removed. Toluene (10 mL) was injected into the flask after cooling to 110 °C in order to prevent solidification of the low melting point solid in the reaction mixture (TOPO). The homogeneous red-brown dispersion was then purified as described below.

Purification involved three centrifugation steps using 50 mL centrifuge tubes. The room temperature product was evenly distributed between four centrifuge tubes, each of which was then diluted to 25 mL with toluene, and precipitated by the addition of 20 mL of ethanol. The mixture was then subjected to centrifugation at 7000 rpm for 5 min, which yielded clear and colorless supernatants and red-brown pellets. The supernatants were then decanted and the pellets dispersed in 20 mL of toluene before addition of 25 mL of ethanol to each. The mixture was then subjected to centrifugation at 7000 rpm for 5 min, which yielded clear and colorless supernatants and red-brown pellets. The supernatants were then decanted and the pellets dispersed in 10 mL of toluene before addition of 35 mL of ethanol to each. The mixture was then subjected to centrifugation at 7000 rpm for 5 min, which yielded red-brown tinted supernatants and red-brown pellets. After this final centrifugation step, the red-brown pellets were dried *in vacuo* at 55 °C overnight to yield 1.097 g (8.15 wt % organics by TGA) of a red-brown solid. CdSe NRs were imaged by TEM (Figure S1) and sized using ImageJ software (L = 40.1 ± 4.1 nm; D = 9.6 ± 1.2 nm).

$Au_{2.6}$-CdSe NR Synthesis. *a. Preparation of CdSe Stock Solution (Au Tip Diameter = 2.6 nm).* To a 20 mL glass scintillation vial equipped with a 1/2″ Teflon coated stir bar was added 60.0 mg of CdSe NRs (40.1 × 9.6 nm; 8.15 wt % organic content by TGA). Toluene (10.0 mL) was then added to the vial to afford a dark red-brown mixture, which was stirred/sonicated until a homogeneous dispersion was obtained.

b. Preparation of Gold Stock Solution (Au Tip Diameter = 2.6 nm). To a 20 mL glass scintillation vial equipped with a 1/2″ Teflon coated stir bar was added gold(III) chloride trihydrate (0.0063 g, 1.6×10^{-5} mol) as the gold precursor, DDAB (0.050 g, 1.1×10^{-4} mol) as a surfactant for the gold salt, and DDA (0.088 g, 4.7×10^{-4} mol) as the reducing agent. Toluene (10.0 mL) was then added to the vial to afford a dark orange-yellow heterogeneous mixture, and the vial was sealed followed by 5 min of sonication, which yielded a light yellow homogeneous solution.

c. Synthesis of Au-CdSe NRs (Au Tip Diameter = 2.6 nm). The synthesis of Au-CdSe NRs was adapted from the literature.[84] A 100 mL three-neck-round-bottom flask equipped with a 1″ glass coated stir bar and a temperature probe was evacuated for 30 min, followed by backfilling with Ar. The CdSe NR stock solution (9.0 mL; described above) was then injected into the flask, after which it was diluted by addition of toluene (36.0 mL). At this point, the gold stock solution (9.0 mL; described above) was injected into the flask over 3 min with continuous stirring (300 rpm) at room temperature (25 °C). The homogeneous red-brown dispersion was then immediately purified as described below.

Purification involved one centrifugation step using 50 mL centrifuge tubes. The room temperature product was evenly distributed between four centrifuge tubes, each of which was then diluted to 25 mL with toluene, and precipitated by the addition of 20 mL of ethanol. The mixture was then subjected to centrifugation at 7000 rpm for 7 min which yielded clear and

colorless supernatants and red-brown pellets. The supernatants were then decanted and the pellets dispersed in 10 mL of DCB. It was noted that the Au-CdSe NRs settled out of solution at a much faster rate than the unmodified rods in similar solvents. At this point, 0.5 mL of the red-brown dispersion was dried *in vacuo* at 55 °C for 24 h in a vial of known mass. This allowed for calculation of the concentration of the dispersion and overall yield, and also provided a powder sample that was utilized for characterization requiring a powder (TGA). For the Au-CdSe NR synthesis reaction described, a typical yield of 57.0 mg (25.52 wt % organics by TGA) was obtained. Au-CdSe NRs were imaged by TEM (see example in Figure S2) from which the degree of Au tipping was found to be highly uniform, with a Au NP diameter of 2.6 nm ±0.5 nm (n = 100). From a total number of 412 rods that were counted, 76% were functionalized with at least one discernible Au NP tip and 24% of the rods were unmodified. These nanorods are denoted $Au_{2.6}$-CdSe NRs.

$Au_{5.6}$-CdSe NR Synthesis. *a. Preparation of CdSe Stock Solution (Au Tip Diameter = 5.6 nm).* To a 20 mL glass scintillation vial equipped with a 1/2″ Teflon coated stir bar was added 18.4 mg of CdSe NRs (40.1 × 9.6 nm; 8.15 wt % organic content by TGA). Toluene (10.0 mL) was then added to the vial to afford a dark red-brown mixture, which was stirred/sonicated until a homogeneous dispersion was obtained.

b. Preparation of Gold Stock Solution (Au Tip Diameter = 5.6 nm). To a 20 mL glass scintillation vial equipped with a 1/2″ Teflon coated stir bar was added gold(III) chloride trihydrate (0.0073 g, 1.9×10^{-5} mol) as the gold precursor, DDAB (0.050 g, 1.1×10^{-4} mol) as a surfactant for the gold salt, and DDA (0.089 g, 4.8×10^{-4} mol) as the reducing agent. Toluene (10.0 mL) was then added to the vial to afford a dark orange-yellow heterogeneous mixture, and the vial was sealed followed by 5 min of sonication, which yielded a light yellow homogeneous solution.

c. Synthesis of Au-CdSe NRs (Au Tip Diameter = 5.6 nm). The synthesis of Au-CdSe NRs was adapted from the literature.[84] A 100 mL three-neck-round-bottom flask equipped with a 1″ glass coated stir bar and a temperature probe was evacuated for 30 min, followed by backfilling with Ar. The CdSe NR stock solution (10.0 mL; described above) was then injected into the flask, after which it was diluted by addition of toluene (30.0 mL). At this point, the gold stock solution (8.0 mL; described above) was injected into the flask over 3 min with continuous stirring (300 rpm) at room temperature (25 °C). The homogeneous red-brown dispersion was then immediately purified in the same manner as previously described for the $Au_{2.6}$-CdSe NRs. A typical yield of 25.4 mg (19.02 wt % organics by TGA) was obtained. Au-CdSe NRs were imaged by TEM (see example in Figure S3), from which Au deposition on the termini as well as the lateral facets of the NRs was observed, with a Au NP diameter of 5.6 nm ±0.9 nm (n = 100). From a total number of 234 rods that were counted, 100.0% were functionalized with at least one discernible Au NP tip and 0% of the rods were unmodified. These nanorods are denoted $Au_{5.6}$-CdSe NRs.

NC Film Preparation and Characterization Methods. Further information on UV−vis, fluorescence, and TGA analysis of NCs, UPS and XPS procedures and data analysis of NR films, and spectroelectrochemical ATR and potential modulated-ATR procedures and data analysis of NR films are presented in SI.

Conflict of Interest: The authors declare no competing financial interest.

Acknowledgment. This material is based upon work supported by the U.S. Department of Energy, Office of Science, Office of Basic Energy Sciences under Award Number DE-FG03-02ER15753. This Award provided the majority of the personnel support. The funding to purchase some of the instrumentation used in this work was provided by the Center for Interface Science: Solar-Electric Materials (CIS:SEM), an Energy Frontier Research Center funded by the U.S. Department of Energy, Office of Basic Energy Sciences under Award Number DE-SC0001084. Additional personnel support was provided by the Arizona Board of Regents TRIF Imaging program (a one-year graduate fellowship for R.E.), and the National Science Foundation under Award Number DMR-130792 (partial salary support for N.G.P.). DMR-130792 also provided partial support for the supplies used in nanomaterial synthesis.

Supporting Information Available: The Supporting Information is available free of charge on the ACS Publications website at DOI: 10.1021/acsnano.5b01720.

TEM and SEM images of NCs and NC films; UV−vis, fluorescence, and TGA analysis of NCs; UPS and XPS procedures and data analysis; spectroelectrochemical ATR and PM-ATR procedures and data analysis. (PDF)

REFERENCES AND NOTES

1. Costi, R.; Cohen, G.; Salant, A.; Rabani, E.; Banin, U. Electrostatic Force Microscopy Study of Single Au−CdSe Hybrid Nanodumbbells: Evidence for Light-Induced Charge Separation. *Nano Lett.* **2009**, *9*, 2031–2039.
2. Costi, R.; Saunders, A. E.; Elmalem, E.; Salant, A.; Banin, U. Visible Light-Induced Charge Retention and Photocatalysis with Hybrid CdSe−Au Nanodumbbells. *Nano Lett.* **2008**, *8*, 637–641.
3. Gao, B.; Lin, Y.; Wei, S.; Zeng, J.; Liao, Y.; Chen, L.; Goldfeld, D.; Wang, X.; Luo, Y.; Dong, Z.; *et al.* Charge Transfer and Retention in Directly Coupled Au-CdSe Nanohybrids. *Nano Res.* **2012**, *5*, 88–98.
4. Govorov, A. O.; Bryant, G. W.; Zhang, W.; Skeini, T.; Lee, J.; Kotov, N. A.; Slocik, J. M.; Naik, R. R. Exciton−Plasmon Interaction and Hybrid Excitons in Semiconductor−Metal Nanoparticle Assemblies. *Nano Lett.* **2006**, *6*, 984–994.
5. Mokari, T.; Rothenberg, E.; Popov, I.; Costi, R.; Banin, U. Selective Growth of Metal Tips Onto Semiconductor Quantum Rods and Tetrapods. *Science* **2004**, *304*, 1787–1790.
6. Steiner, D.; Mokari, T.; Banin, U.; Millo, O. Electronic Structure of Metal-Semiconductor Nanojunctions in Gold CdSe Nanodumbbells. *Phys. Rev. Lett.* **2005**, *95*, 056805.
7. Yu, P.; Wen, X.; Lee, Y.-C.; Lee, W.-C.; Kang, C.-C.; Tang, J. Photoinduced Ultrafast Charge Separation in Plexcitonic CdSe/Au and CdSe/Pt Nanorods. *J. Phys. Chem. Lett.* **2013**, *4*, 3596–3601.
8. Li, Z.; Hu, Y.; Sun, Y. Promoting Photocatalytic Multiple-Electron Reduction in Aerobic Solutions Using Au-Tipped CdSe Nanorod Clusters. *Chem. Commun.* **2014**, *50*, 1411–1413.
9. Chamousis, R. L.; Osterloh, F. E. Use of Potential Determining Ions to Control Energetics and Photochemical Charge Transfer of a Nanoscale Water Splitting Photocatalyst. *Energy Environ. Sci.* **2014**, *7*, 736–743.
10. Osterloh, F. E. Inorganic Nanostructures for Photoelectrochemical and Photocatalytic Water Splitting. *Chem. Soc. Rev.* **2013**, *42*, 2294–2320.
11. Osterloh, F. E. Boosting the Efficiency of Suspended Photocatalysts for Overall Water Splitting. *J. Phys. Chem. Lett.* **2014**, *5*, 2510–2511.
12. Wu, K.; Chen, Z.; Lv, H.; Zhu, H.; Hill, C. L.; Lian, T. Hole Removal Rate Limits Photodriven H_2 Generation Efficiency in CdS-Pt and CdSe/CdS-Pt Semiconductor Nanorod-Metal Tip Heterostructures. *J. Am. Chem. Soc.* **2014**, *136*, 7708–7716.
13. Wu, K.; Rodriguez-Cordoba, W.; Lian, T. Exciton Localization and Dissociation Dynamics in CdS and CdS-Pt Quantum Confined Nanorods: Effect of Nonuniform Rod Diameters. *J. Phys. Chem. B* **2014**, *118*, 14062–14069.
14. Zhu, H.; Song, N.; Lv, H.; Hill, C. L.; Lian, T. Near Unity Quantum Yield of Light-Driven Redox Mediator Reduction and Efficient H_2 Generation Using Colloidal Nanorod Heterostructures. *J. Am. Chem. Soc.* **2012**, *134*, 11701–11708.
15. Warren, E. L.; Atwater, H. A.; Lewis, N. S. Silicon Microwire Arrays for Solar Energy-Conversion Applications. *J. Phys. Chem. C* **2014**, *118*, 747–759.
16. Hu, S.; Chi, C. Y.; Fountaine, K. T.; Yao, M. Q.; Atwater, H. A.; Dapkus, P. D.; Lewis, N. S.; Zhou, C. W. Optical, Electrical, and Solar Energy-Conversion Properties of Gallium Arsenide Nanowire-Array Photoanodes. *Energy Environ. Sci.* **2013**, *6*, 1879–1890.
17. Tarafder, K.; Surendranath, Y.; Olshansky, J. H.; Alivisatos, A. P.; Wang, L.-W. Hole Transfer Dynamics from a CdSe/CdS

Quantum Rod to a Tethered Ferrocene Derivative. *J. Am. Chem. Soc.* **2014**, *136*, 5121–5131.
18. Thorkelsson, K.; Nelson, J. H.; Alivisatos, A. P.; Xu, T. End-to-End Alignrnent of Nanorods in Thin Films. *Nano Lett.* **2013**, *13*, 4908–4913.
19. Hughes, S. M.; Alivisatos, A. P. Anisotropic Formation and Distribution of Stacking Faults in II-VI Semiconductor Nanorods. *Nano Lett.* **2013**, *13*, 106–110.
20. Soreni-Harari, M.; Yaacobi-Gross, N.; Steiner, D.; Aharoni, A.; Banin, U.; Millo, O.; Tessler, N. Tuning Energetic Levels in Nanocrystal Quantum Dots Through Surface Manipulations. *Nano Lett.* **2008**, *8*, 678–684.
21. Li, J.; Cushing, S. K.; Zheng, P.; Senty, T.; Meng, F.; Bristow, A. D.; Manivannan, A.; Wu, N. Solar Hydrogen Generation by a CdS-Au-TiO_2 Sandwich Nanorod Array Enhanced with Au Nanoparticle as Electron Relay and Plasmonic Photosensitizer. *J. Am. Chem. Soc.* **2014**, *136*, 8438–8449.
22. Menagen, G.; Macdonald, J. E.; Shemesh, Y.; Popov, I.; Banin, U. Au Growth on Semiconductor Nanorods: Photoinduced *versus* Thermal Growth Mechanisms. *J. Am. Chem. Soc.* **2009**, *131*, 17406–17411.
23. Katz, D.; Wizansky, T.; Millo, O.; Rothenberg, E.; Mokari, T.; Banin, U. Size-Dependent Tunneling and Optical Spectroscopy of CdSe Quantum Rods. *Phys. Rev. Lett.* **2002**, *89*, 086801.
24. Figuerola, A.; van Huis, M.; Zanella, M.; Genovese, A.; Marras, S.; Falqui, A.; Zandbergen, H. W.; Cingolani, R.; Manna, L. Epitaxial CdSe-Au Nanocrystal Heterostructures by Thermal Annealing. *Nano Lett.* **2010**, *10*, 3028–3036.
25. Maiolo, J. R.; Kayes, B. M.; Filler, M. A.; Putnam, M. C.; Kelzenberg, M. D.; Atwater, H. A.; Lewis, N. S. High Aspect Ratio Silicon Wire Array Photoelectrochemical Cells. *J. Am. Chem. Soc.* **2007**, *129*, 12346–12347.
26. Kelzenberg, M. D.; Boettcher, S. W.; Petykiewicz, J. A.; Turner-Evans, D. B.; Putnam, M. C.; Warren, E. L.; Spurgeon, J. M.; Briggs, R. M.; Lewis, N. S.; Atwater, H. A. Enhanced Absorption and Carrier Collection in Si Wire Arrays for Photovoltaic Applications. *Nat. Mater.* **2010**, *9*, 239–244.
27. Tamboli, A. C.; Chen, C. T.; Warren, E. L.; Turner-Evans, D. B.; Kelzenberg, M. D.; Lewis, N. S.; Atwater, H. A. Wafer-Scale Growth of Silicon Microwire Arrays for Photovoltaics and Solar Fuel Generation. *IEEE J. Photovolt.* **2012**, *2*, 294–297.
28. Shallcross, R. C.; D'Ambruoso, G. D.; Korth, B. D.; Hall, H. K.; Zheng, Z. P.; Pyun, J.; Armstrong, N. R. Poly(3,4-ethylenedioxythiophene) - Semiconductor Nanoparticle Composite Thin Films Tethered to Indium Tin Oxide Substrates *via* Electropolymerization. *J. Am. Chem. Soc.* **2007**, *129*, 11310–11311.
29. Shallcross, R. C.; D'Ambruoso, G. D.; Pyun, J.; Armstrong, N. R. Photoelectrochemical Processes in Polymer-Tethered CdSe Nanocrystals. *J. Am. Chem. Soc.* **2010**, *132*, 2622–2632.
30. Carlson, B.; Leschkies, K.; Aydil, E. S.; Zhu, X. Y. Valence Band Alignment at Cadmium Selenide Quantum Dot and Zinc Oxide ($10\bar{1}0$) Interfaces. *J. Phys. Chem. C* **2008**, *112*, 8419–8423.
31. Li, R.; Cai, C.; Hu, L.; Wu, H.; Zhang, W.; Zhu, J. Band Alignment of ZnO/CdSe Quantum Dots Heterojunction Determined by Ultraviolet Photoelectron Spectroscopy Using Synchrotron Radiation. *Appl. Surf. Sci.* **2013**, *276*, 258–261.
32. Timp, B. A.; Zhu, X. Y. Electronic Energy Alignment at the PbSe Quantum Dots/ZnO($10\bar{1}0$) Interface. *Surf. Sci.* **2010**, *604*, 1335–1341.
33. Boehme, S. C.; Wang, H.; Siebbeles, L. D. A.; Vanmaekelbergh, D.; Houtepen, A. J. Electrochemical Charging of CdSe Quantum Dot Films: Dependence on Void Size and Counterion Proximity. *ACS Nano* **2013**, *7*, 2500–2508.
34. Jasieniak, J.; Califano, M.; Watkins, S. E. Size-Dependent Valence and Conduction Band-Edge Energies of Semiconductor Nanocrystals. *ACS Nano* **2011**, *5*, 5888–5902.
35. Araci, Z. O.; Shallcross, C. R.; Armstrong, N. R.; Saavedra, S. S. Potential-Modulated Attenuated Total Reflectance Characterization of Charge Injection Processes in Monolayer-Tethered CdSe Nanocrystals. *J. Phys. Chem. Lett.* **2010**, *1*, 1900–1905.
36. Munro, A. M.; Zacher, B.; Graham, A.; Armstrong, N. R. Photoemission Spectroscopy of Tethered CdSe Nanocrystals: Shifts in Ionization Potential and Local Vacuum Level as a Function of Nanocrystal Capping Ligand. *ACS Appl. Mater. Interfaces* **2010**, *2*, 863–869.
37. Colvin, V. L.; Alivisatos, A. P.; Tobin, J. G. Valence-Band Photoemission From a Quantum-Dot System. *Phys. Rev. Lett.* **1991**, *66*, 2786–2789.
38. Markus, T. Z.; Itzhakov, S.; Akotzer, Y. I.; Cahen, D.; Hodes, G.; Oron, D.; Naaman, R. Energetics of CdSe Quantum Dots Adsorbed on TiO_2. *J. Phys. Chem. C* **2011**, *115*, 13236–13241.
39. Markus, T. Z.; Wu, M.; Wang, L.; Waldeck, D. H.; Oron, D.; Naaman, R. Electronic Structure of CdSe Nanoparticles Adsorbed on Au Electrodes by an Organic Linker: Fermi Level Pinning of the HOMO. *J. Phys. Chem. C* **2009**, *113*, 14200–14206.
40. Wang, Y.; Xie, Z.; Gotesman, G.; Wang, L.; Bloom, B. P.; Markus, T. Z.; Oron, D.; Naaman, R.; Waldeck, D. H. Determination of the Electronic Energetics of CdTe Nanoparticle Assemblies on Au Electrodes by Photoemission, Electrochemical, and Photocurrent Studies. *J. Phys. Chem. C* **2012**, *116*, 17464–17472.
41. Bussolotti, F.; Kera, S.; Kudo, K.; Kahn, A.; Ueno, N. Gap States in Pentacene Thin Film Induced by Inert Gas Exposure. *Phys. Rev. Lett.* **2013**, *110*, 267602.
42. Sueyoshi, T.; Kakuta, H.; Ono, M.; Sakamoto, K.; Kera, S.; Ueno, N. Band Gap States of Copper Phthalocyanine Thin Films Induced by Nitrogen Exposure. *Appl. Phys. Lett.* **2010**, *96*, 093303.
43. Hughes, B. K.; Luther, J. M.; Beard, M. C. The Subtle Chemistry of Colloidal, Quantum-Confined Semiconductor Nanostructures. *ACS Nano* **2012**, *6*, 4573–4579.
44. Hughes, B. K.; Ruddy, D. A.; Blackburn, J. L.; Smith, D. K.; Bergren, M. R.; Nozik, A. J.; Johnson, J. C.; Beard, M. C. Control of PbSe Quantum Dot Surface Chemistry and Photophysics Using an Alkylselenide Ligand. *ACS Nano* **2012**, *6*, 5498–5506.
45. Weiss, E. A. Organic Molecules as Tools to Control the Growth, Surface Structure, and Redox Activity of Colloidal Quantum Dots. *Acc. Chem. Res.* **2013**, *46*, 2607–2615.
46. Greaney, M. J.; Das, S.; Webber, D. H.; Bradforth, S. E.; Brutchey, R. L. Improving Open Circuit Potential in Hybrid P3HT:CdSe Bulk Heterojunction Solar Cells *via* Colloidal tert-Butylthiol Ligand Exchange. *ACS Nano* **2012**, *6*, 4222–4230.
47. Wang, C.; Shim, M.; Guyot-Sionnest, P. Electrochromic Nanocrystal Quantum Dots. *Science* **2001**, *291*, 2390–2392.
48. Hou, B.; Parker, D.; Kissling, G. P.; Jones, J. A.; Cherns, D.; Fermin, D. J. Structure and Band Edge Energy of Highly Luminescent $CdSe_{1-x}Te_x$ Alloyed Quantum Dots. *J. Phys. Chem. C* **2013**, *117*, 6814–6820.
49. Mukherjee, S.; Hazarika, A.; Santra, P. K.; Abdelhady, A. L.; Malik, M. A.; Gorgoi, M.; O'Brien, P.; Karis, O.; Sarma, D. D. Determination of Internal Structures of Heterogeneous Nanocrystals Using Variable-Energy Photoemission Spectroscopy. *J. Phys. Chem. C* **2014**, *118*, 15534–15540.
50. Xiong, W.; Hickstein, D. D.; Schnitzenbaumer, K. J.; Ellis, J. L.; Palm, B. B.; Keister, K. E.; Ding, C.; Miaja-Avila, L.; Dukovic, G.; Jimenez, J. L.; *et al.* Photoelectron Spectroscopy of CdSe Nanocrystals in the Gas Phase: A Direct Measure of the Evanescent Electron Wave Function of Quantum Dots. *Nano Lett.* **2013**, *13*, 2924–2930.
51. Doherty, W. J., III; Donley, C. L.; Armstrong, N. R.; Saavedra, S. S. A Broadband Spectroelectrochemical ATR Instrument for Molecular Adlayer Studies. *Appl. Spectrosc.* **2002**, *56*, 920–927.
52. Dunphy, D. R.; Mendes, S. B.; Saavedra, S. S.; Armstrong, N. R. The Electroactive Integrated Optical Waveguide (EA-IOW): Ultrasensitive Spectroelectrochemistry of Submonolayer Adsorbates. *Anal. Chem.* **1997**, *69*, 3086–3094.
53. Kelly, C. P.; Cramer, C. J.; Truhlar, D. G. Single-Ion Solvation Free Energies and the Normal Hydrogen Electrode Potential in Methanol, Acetonitrile, and Dimethyl Sulfoxide. *J. Phys. Chem. B* **2006**, *111*, 408–422.

54. Guyot-Sionnest, P.; Wang, C. Fast Voltammetric and Electrochromic Response of Semiconductor Nanocrystal Thin Films. *J. Phys. Chem. B* **2003**, *107*, 7355–7359.
55. Guyot-Sionnest, P. Charging Colloidal Quantum Dots by Electrochemistry. *Microchim. Acta* **2008**, *160*, 309–314.
56. Khon, E.; Mereshchenko, A.; Tarnovsky, A. N.; Acharya, K.; Klinkova, A.; Hewa-Kasakarage, N. N.; Nemitz, I.; Zamkov, M. Suppression of the Plasmon Resonance in Au/CdS Colloidal Nanocomposites. *Nano Lett.* **2011**, *11*, 1792–1799.
57. Hill, L. J.; Bull, M. M.; Sung, Y.; Simmonds, A. G.; Dirlam, P. T.; Richey, N. E.; DeRosa, S. E.; Shim, I.-B.; Guin, D.; Costanzo, P. J.; *et al.* Directing the Deposition of Ferromagnetic Cobalt Onto Pt-Tipped CdSe@CdS Nanorods: Synthetic and Mechanistic Insights. *ACS Nano* **2012**, *6*, 8632–8645.
58. Carbone, L.; Nobile, C.; De Giorgi, M.; Sala, F. D.; Morello, G.; Pompa, P.; Hytch, M.; Snoeck, E.; Fiore, A.; Franchini, I. R.; *et al.* Synthesis and Micrometer-Scale Assembly of Colloidal CdSe/CdS Nanorods Prepared by a Seeded Growth Approach. *Nano Lett.* **2007**, *7*, 2942–2950.
59. Seah, M. P.; Dench, W. A. Quantitative Electron Spectroscopy of Surfaces: A Standard Data Base for Electron Inelastic Mean Free Paths in Solids. *Surf. Interface Anal.* **1979**, *1*, 2–11.
60. Alloway, D. M.; Graham, A. L.; Yang, X.; Mudalige, A.; Colorado, R.; Wysocki, V. H.; Pemberton, J. E.; Lee, T. R.; Wysocki, R. J.; Armstrong, N. R. Tuning the Effective Work Function of Gold and Silver Using omega-Functionalized Alkanethiols: Varying Surface Composition through Dilution and Choice of Terminal Groups. *J. Phys. Chem. C* **2009**, *113*, 20328–20334.
61. Alloway, D. M.; Hofmann, M.; Smith, D. L.; Gruhn, N. E.; Graham, A. L.; Colorado, R.; Wysocki, V. H.; Lee, T. R.; Lee, P. A.; Armstrong, N. R. Interface Dipoles Arising From Self-Assembled Monolayers on Gold: UV-Photoemission Studies of Alkanethiols and Partially Fluorinated Alkanethiols. *J. Phys. Chem. B* **2003**, *107*, 11690–11699.
62. Cahen, D.; Kahn, A. Electron Energetics at Surfaces and Interfaces: Concepts and Experiments. *Adv. Mater.* **2003**, *15*, 271–277.
63. Yi, Y.; Lyon, J. E.; Beerbom, M. M.; Schlaf, R. Orbital Alignment at Poly 2-methoxy-5-(2(')-ethylhexyloxy)-p-Phenylene Vinylene Interfaces. *J. Appl. Phys.* **2007**, *102*, 023710.
64. Cascio, A. J.; Lyon, J. E.; Beerbom, M. M.; Schlaf, R.; Zhu, Y.; Jenekhe, S. A. Investigation of a Polythiophene Interface Using Photoemission Spectroscopy in Combination with Electrospray Thin-Film Deposition. *Appl. Phys. Lett.* **2006**, *88*, 062104.
65. Schroeder, P. G.; France, C. B.; Parkinson, B. A.; Schlaf, R. Orbital Alignment at p-Sexiphenyl and Coronene/Layered Materials Interfaces Measured with Photoemission Spectroscopy. *J. Appl. Phys.* **2002**, *91*, 9095–9107.
66. Magulick, J.; Beerbom, M. M.; Schlaf, R. Comparison of Ribonucleic Acid Homopolymer Ionization Energies and Charge Injection Barriers. *J. Phys. Chem. B* **2006**, *110*, 15973–15981.
67. Magulick, J.; Beerbom, M. M.; Lagel, B.; Schlaf, R. Ionization Energy and Electronic Structure of Polycytidine. *J. Phys. Chem. B* **2006**, *110*, 2692–2699.
68. Schlaf, R.; Parkinson, B. A.; Lee, P. A.; Nebesny, K. W.; Armstrong, N. R. Absence of Final-State Screening Shifts in Photoemission Spectroscopy Frontier Orbital Alignment Measurements at Organic/Semiconductor Interfaces. *Surf. Sci.* **1999**, *420*, L122–L129.
69. Li, X. M.; Zhang, Z. M.; Henrich, V. E. Inelastic Electron Background Function for Ultraviolet Photoelectron-Spectra. *J. Electron Spectrosc. Relat. Phenom.* **1993**, *63*, 253–265.
70. Lee, J. R. I.; Meulenberg, R. W.; Hanif, K. M.; Mattoussi, H.; Klepeis, J. E.; Terminello, L. J.; van Buuren, T. Experimental Observation of Quantum Confinement in the Conduction Band of CdSe Quantum Dots. *Phys. Rev. Lett.* **2007**, *98*, 146803.
71. Meulenberg, R. W.; Lee, J. R. I.; Wolcott, A.; Zhang, J. Z.; Terminello, L. J.; van Buuren, T. Determination of the Exciton Binding Energy in CdSe Quantum Dots. *ACS Nano* **2009**, *3*, 325–330.
72. Wright, J. T.; Meulenberg, R. W. Modification of the Conduction Band Edge Energy *via* Hybridization in Quantum Dots. *Appl. Phys. Lett.* **2012**, *101*, 193104.
73. Banin, U.; Millo, O. Tunneling and Optical Spectroscopy of Semiconductor Nanocrystals. *Annu. Rev. Phys. Chem.* **2003**, *54*, 465–492.
74. Zhang, Y.; Pluchery, O.; Caillard, L.; Lamic-Humblot, A. F.; Casale, S.; Chabal, Y. J.; Salmeron, M. Sensing the Charge State of Single Gold Nanoparticles *via* Work Function Measurements. *Nano Lett.* **2015**, *15*, 51–55.
75. Lin, H.-C.; Polaske, N. W.; Oquendo, L. E.; Gliboff, M.; Knesting, K. M.; Nordlund, D.; Ginger, D. S.; Ratcliff, E. L.; Beam, B. M.; Armstrong, N. R.; *et al.* Electron-Transfer Processes in Zinc Phthalocyanine−Phosphonic Acid Monolayers on ITO: Characterization of Orientation and Charge-Transfer Kinetics by Waveguide Spectroelectrochemistry. *J. Phys. Chem. Lett.* **2012**, *3*, 1154–1158.
76. Inamdar, S. N.; Ingole, P. P.; Haram, S. K. Determination of Band Structure Parameters and the Quasi-Particle Gap of CdSe Quantum Dots by Cyclic Voltammetry. *ChemPhysChem* **2008**, *9*, 2574–2579.
77. Houtepen, A. J.; Vanmaekelbergh, D. Orbital Occupation in Electron-Charged CdSe Quantum-Dot Solids. *J. Phys. Chem. B* **2005**, *109*, 19634–19642.
78. Shabaev, A.; Efros, A. L. 1D Exciton Spectroscopy of Semiconductor Nanorods. *Nano Lett.* **2004**, *4*, 1821–1825.
79. Efros, A. L.; Rosen, M. The Electronic Structure of Semiconductor Nanocrystals. *Annu. Rev. Mater. Sci.* **2000**, *30*, 475–521.
80. Cardona, C. M.; Li, W.; Kaifer, A. E.; Stockdale, D.; Bazan, G. C. Electrochemical Considerations for Determining Absolute Frontier Orbital Energy Levels of Conjugated Polymers for Solar Cell Applications. *Adv. Mater.* **2011**, *23*, 2367–2371.
81. Saraf, D.; Kshirsagar, A. Electronic Structure at Nanocontacts of Surface Passivated CdSe Nanorods with Gold Clusters. *Phys. Chem. Chem. Phys.* **2014**, *16*, 10823–10829.
82. Plowman, T. E.; Saavedra, S. S.; Reichert, W. M. Planar Integrated Optical Methods for Examining Thin Films and Their Surface Adlayers. *Biomaterials* **1998**, *19*, 341–355.
83. Yu, W. W.; Qu, L. H.; Guo, W. Z.; Peng, X. G. Experimental Determination of the Extinction Coefficient of CdTe, CdSe, and CdS Nanocrystals. *Chem. Mater.* **2003**, *15*, 2854–2860.
84. Mokari, T.; Sztrum, C. G.; Salant, A.; Rabani, E.; Banin, U. Formation of Asymmetric One-Sided Metal-Tipped Semiconductor Nanocrystal Dots and Rods. *Nat. Mater.* **2005**, *4*, 855–863.